

Article

Remote Sensing of Organic Films on the Water Surface Using Dual Co-Polarized Ship-Based X-/C-/S-Band Radar and TerraSAR-X

Stanislav A. Ermakov ^{1,*}, Irina A. Sergievskaya ¹, José C.B. da Silva ² , Ivan A. Kapustin ¹ ,
Olga V. Shomina ¹, Alexander V. Kupaev ¹ and Alexander A. Molkov ¹ 

¹ Institute of Applied Physics, Russian Academy of Sciences, 46 Uljanova St., 603950 Nizhny Novgorod, Russia; onw2009@mail.ru (I.A.S.); kapustin-i@yandex.ru (I.A.K.); seamka@yandex.ru (O.V.S.); sant3@mail.ru (A.V.K.); wave3d@mail.ru (A.A.M.);

² Department of Geoscience, Environment & Spatial Planning, University of Porto, Rua do Campo Alegre, 687, 4169-007 Porto, Portugal; jdasilva@fc.up.pt

* Correspondence: stas.ermakov8@gmail.com; Tel.: +7-831-416-4935

Received: 30 April 2018; Accepted: 5 July 2018; Published: 10 July 2018



Abstract: Microwave radar is a well-established tool for all-weather monitoring of film slicks which appear in radar imagery of the surface of water bodies as areas of reduced backscatter due to suppression of short wind waves. Information about slicks obtained with single-band/one-polarized radar seems to be insufficient for film characterization; hence, new capabilities of multi-polarization radars for monitoring of film slicks have been actively discussed in the literature. In this paper the results of new experiments on remote sensing of film slicks using dual co-polarized radars—a satellite TerraSAR-X and a ship-based X-/C-/S-band radar—are presented. Radar backscattering is assumed to contain Bragg and non-Bragg components (BC and NBC, respectively). BC is due to backscattering from resonant cm-scale wind waves, while NBC is supposed to be associated with wave breaking. Each of the components can be eliminated from the total radar backscatter measured at two co-polarizations, and contrasts of Bragg and non-Bragg components in slicks can be analyzed separately. New data on a damping ratio (contrast) characterizing reduction of radar returns in slicks are obtained for the two components of radar backscatter in various radar bands. The contrast values for Bragg and non-Bragg components are comparable to each other and demonstrate similar dependence on radar wave number; BC and NBC contrasts grow monotonically for the cases of upwind and downwind observations and weakly decrease with wave number for the cross-wind direction. Reduction of BC in slicks can be explained by enhanced viscous damping of cm-scale Bragg waves due to an elastic film. Physical mechanisms of NBC reduction in slicks are discussed. It is hypothesized that strong breaking (e.g., white-capping) weakly contributes to the NBC contrast because of “cleaning” of the water surface due to turbulent surfactant mixing associated with wave crest overturning. An effective mechanism of NBC reduction due to film can be associated with modification of micro-breaking wave features, such as parasitic ripples, bulge, and toe, in slicks.

Keywords: remote sensing; film slicks on the sea surface; dual co-polarized microwave radar; surface wind waves; wave breaking

1. Introduction

Pollution of the sea surface is an imminent threat for the ecological state of open ocean, coastal zones, and inland waters. Remote sensing of marine films, both biogenic pollutions and oil spills, is aimed to identify the films and to quantify their characteristics, and is a very important and urgent problem actively discussed in the literature (see, [1–7], and references therein). This problem, however,

is still far from a comprehensive solution. Microwave radar, as a day-and-night/all-weather tool, is particularly interesting for remote sensing of the sea surface. Slicks, associated with surfactants and/or mineral oil films can be easily detected, basically at low-to-moderate wind speeds, using both side-looking real aperture radar (RAR) onboard ships, aircrafts and marine platforms, and satellite synthetic aperture radar (SAR) (see, e.g., [4–7]). Film slicks appear in radar imagery of the sea surface as areas of reduced radar backscatter, and the latter is essentially a result of enhanced suppression of short wind waves.

One of the difficulties to resolve the problem is that mechanisms of suppression of wind waves by films are still not completely understood, particularly for crude oil films. Theoretical analysis has shown that the wave damping coefficient depends on physical characteristics of surface films, such as the surface tension and film elasticity (or viscoelasticity) for monomolecular surfactant films (see e.g., [8–10]), and on the surface and interfacial tensions and viscoelasticities, as well as the volume viscosity for oil layers of finite thickness (“thick oil films”) [11,12]. The physical characteristics for monomolecular organic films were experimentally investigated in detail in [13–15], while properties of “thick” oil films have been studied insufficiently (see, [12,16]).

Another difficulty is how to correctly describe the action of films on short wind waves, keeping in mind that physical mechanisms of generation of wind waves, their nonlinear interactions and dissipation, and, hence, formation of the wind wave spectrum are poorly known and parameterized. As a result, existing models of the wind wave spectrum [17–20] are mostly empirical and cannot be considered as very reliable.

The third difficulty is that the very mechanisms of microwave scattering at the sea surface are still under investigation and existing models of radar returns cannot explain experiments properly. Conventional models, a Bragg scattering model and its extended version—a two-scale model (see, e.g., [21,22])—are unable, in general, to explain some important characteristics of microwave radar returns. In particular, it has been demonstrated in [23] when analyzing TerraSAR-X and Envisat ASAR VV-polarized images that reduction of radar return (radar contrast) in film slicks at incidence angles from 20° to 40°, and at low-to-moderate wind, is relatively weak (about 2–3 times) and almost independent both on incidence angle and film elasticity. A conventional composite radar model, taking into account Bragg (resonance) and specular (Kirchhoff) scattering mechanisms [21,22] has underestimated the radar contrast at incidence angles less than 25–30° and overestimated the contrasts at larger angles [23]. A possible reason of the model drawbacks is the existence of an additional component of radar returns, associated with breaking of wind waves, as it has been hypothesized in [24]. This hypothesis is supported, first of all, by the occurrence of strong “spikes” in radar returns, particularly in HH-polarization, which are not consistent with the Bragg scattering mechanism [25–27]. Secondly, experimentally measured values of a ratio of radar backscatter at VV and HH polarizations are smaller than those predicted by a two-scale model. The third inconsistency is that microwave radar Doppler shifts do not accurately correspond to the phase velocities of linear gravity-capillary Bragg waves. This may indicate that so-called bound or parasitic waves, which are generated by breaking waves, longer than Bragg ones, contribute to the radar Doppler shifts (see, e.g., [28–30]).

In [20] a physical radar model has been developed, following the hypothesis of [24], that the radar return is a sum of a Bragg (“polarized”) component and a non-Bragg (“non-polarized”) component, the latter appearing due to quasi-specular reflection from some facets on the profile of steep (breaking) waves. The non-Bragg component (NBC) has been described as similar to a Kirchhoff specular scattering model with some empirical coefficients. The latter have been introduced to make the model consistent with experiment, largely limited to C-band radar observations. It has been suggested in [31] to analyze different combinations of VV and HH signals, such as the polarization difference (PD) and polarization ratio (PR), thus eliminating either Bragg or non-Bragg backscatter components from the total radar return. The two components respond differently on non-uniform currents, low wind areas, slicks, etc., and potential capabilities to emphasize that one or the other surface signature in radar imagery can be realized. In particular, to develop more effective approaches to solve the problem of

film slick remote sensing some observations with dual- and quad-polarized single-band radars have been carried out (see, e.g., [31–33]). In [32] where Radarsat (RS) and TerraSAR-X (TS) acquisitions of slicks were analyzed any noticeable effect of surface film on the non-Bragg component was not revealed. However, a significant reduction of NBC in films slicks was reported later in [33]. It was obtained in [33], based on analysis of Radarsat-2 observations, that NBC and BC contrasts in film slicks of different origin are comparable to each other.

A limitation of the experiments was the use of single band radars and poor knowledge of slick properties (film elasticity, surface tension, viscosity, etc.), responsible for suppression of wind waves. Accordingly, further, more detailed, quantitative studies of different components of radar return from the areas covered with films are needed for better understanding of mechanisms of slick radar imaging and for elaboration of models and methods of slick detection and identification. In the context of the problem solution it is crucially important (a) to check whether damping of Bragg waves can be described by hydrodynamic theory which predicts the damping as a function of film parameters, and (b) to understand how breaking wave features, i.e., crest overturning and micro-breaking, are modified by film. As it was mentioned above, dependences of wave damping on film characteristics (and on wave number, too) were studied, e.g., in [12–16]. Films with pre-measured surface tension and elasticity can be used as calibrated ones in experiment to study, in particular, reduction of BC due to damping of Bragg waves. As for the modification of steep wave profiles due to films, which might be responsible for the reduction of non-Bragg radar returns, the problem is practically open. Wave tank experiments [34] revealed that the film was destroyed in the area of spilling wave breakers, which resulted in “cleaning” of the water surface in the vicinity of breaking crests of m-scale waves. Accordingly, one can assume that strong wave breaking of m-scale waves weakly contributes to the reduction of the non-Bragg radar component, and modification of micro-breaking of cm-dm-scale waves in slicks can play the most important role in non-Bragg contrasts in slicks. The latter is characterized by the appearance near wave crests of structures with high curvature, so-called bulge and toe [35], and by parasitic capillary ripples [36,37] propagating on the forward slopes of steep waves.

This paper presents new results of studies of film slicks using dual co-polarized radar: the satellite TerraSAR-X and an X-/C-/S-band scatterometer mounted onboard a research vessel. The paper is organized as follows: Section 2 presents the theoretical background, introducing Bragg and non-Bragg scattering components and their extraction from the total normalized radar cross-section (NRCS) at VV and HH polarizations. Section 2 also describes the apparatus and methodology of the experiments on radar probing of slicks formed by “calibrated” organic films. The obtained experimental results are presented in Section 3, and possible physical mechanisms responsible for suppression of Bragg and non-Bragg radar components are discussed in Section 4. Conclusions are given in Section 5.

2. Materials and Methods

2.1. Theoretical Background

Radar observations of the sea surface indicate that microwave backscattering is characterized by the occurrence of short pulses (spikes) which are significantly larger than some mean (“background”) level between the spikes. The latter, as it has been hypothesized in [24], can be associated with breaking of wind waves (either micro- or strong breaking), while the lower background level corresponds basically to Bragg scattering. Thus, the total NRCS was supposed to be a sum of Bragg and non-Bragg components:

$$\sigma_{pp}^0 = \sigma_{BC_pp} + \sigma_{NBC} \quad (1)$$

where σ_{pp}^0 is the total NRCS, p denotes vertical (V), or horizontal (H) transmit/receive polarizations, σ_{BC_pp} is the Bragg (VV or HH) component of NRCS described by the two-scale model, σ_{NBC} denotes the NBC associated with quasi-specular scattering from surface facets on micro- or strong wave breakers.

The Bragg component, according to a two-scale radar model (see, e.g., [21,22]) can be expressed as:

$$\sigma_{BC_pp}^0 = 16\pi k_{em}^4 R_{pp}(\theta) F(\vec{k}_B) \quad (2)$$

where $F(\vec{k}_B)$ is the spectrum of wind waves at a Bragg wave vector $\vec{k}_B = 2k_{em}\vec{n}_s$, k_{em} is the wave number of an incident electromagnetic wave, \vec{n}_s is a projection of the unit wave vector of the incident wave on the sea surface, $|\vec{n}_s| = \sin\theta$, θ is an incidence angle, $R_{pp}(\theta)$ is a reflection coefficient which depends on polarizations of the incident/reflected electromagnetic waves, and in general on root mean square (r.m.s.) slopes of long surface waves, i.e., those which are longer than the antenna footprint [21]. Non-Bragg scattering from the areas of wave breaking is assumed to be independent of polarization, and σ_{NBC} is characterized in the literature as non-polarized.

It has been suggested in [31] to remove the NBC from the total NRCS when subtracting σ_{HH}^0 from σ_{VV}^0 . Thus obtained backscatter polarization difference σ_{PD} is:

$$\sigma_{PD} = \sigma_{VV}^0 - \sigma_{HH}^0 = \sigma_{BC_VV}^0 - \sigma_{BC_HH}^0 = (R_{VV} - R_{HH})F(\vec{k}_B) \quad (3)$$

The non-Bragg radar backscatter component, σ_{NBC} can be found from Equations (1) and (3) as:

$$\sigma_{NBC} = \sigma_{VV}^0 - (\sigma_{VV}^0 - \sigma_{HH}^0)/(1 - R_{HH}/R_{VV}) \quad (4)$$

Slick contrasts for the total NRCS, Bragg and non-Bragg components are defined as:

$$K_{pp} = \frac{\sigma_{pp_nonslick}^0}{\sigma_{pp_slick}^0}, K_{BC} = K_{PD} = \frac{\sigma_{PD_nonslick}^0}{\sigma_{PD_slick}^0}, K_{NBC} = \frac{\sigma_{NBC_nonslick}^0}{\sigma_{NBC_slick}^0} \quad (5)$$

Since the polarization difference is supposedly proportional to the Bragg components of NRCS, the contrast K_{PD} is equal to BC contrast K_{BC} . If one assumes that that film does not affect the scattering coefficients R_{VV} and R_{HH} , then the BC contrast is determined by the wind wave spectrum outside/inside slick $K_{PD} = F_{nonslick}(k_B)/F_{slick}(k_B)$. Transformation of the spectrum of short wind waves due to film can be considered in the frame of a local balance model in [2,4,18], or using an improved physical model [20]. Without going into detail it can be said that the BC contrast for both the models depends on the energy sources, sinks, and nonlinear terms in the kinetic equation for the wind wave spectrum. In a particular case of low wind wave input that is realized, e.g., for wind wave components propagating across the wind, the BC contrast can be expressed as a ratio γ_s/γ_{nsl} of surface wave damping coefficients inside the slick (s) and in a surrounding non slick area (nsl). The ratio γ_s/γ_{nsl} can be described using the theory of wave damping in the presence of an elastic film (see, e.g., [8–10]). Then the BC contrast for the cross wind direction is:

$$K_{BC}(crosswind) \approx \gamma_s/\gamma_0 = \frac{1 - X + XY}{1 - 2X + 2X^2} \quad (6)$$

where $X = \frac{Ek^2}{\rho(2\nu)^{1/2}\omega^{3/2}}$ and $Y = \frac{Ek}{4\rho\nu\omega}$. Here ρ denotes the water density, ν the kinematic water viscosity, E the film elasticity, k and ω are the wave frequency and wave number of the wind wave spectrum component, respectively.

2.2. Experiment

Experiments on radar probing of film slicks were carried out in the southern part of the Gorky Water Reservoir (GWR) of the Volga River, Nizhny Novgorod Region, Russia. GWR extends approximately from north to south for about 100 km, and its width is 5–15 km. Artificial film slicks in the experiments of 2014 and 2015 were observed with satellite TerraSAR-X operating at a frequency of 9.65 GHz. Experiments of 2016 were performed using a new three-band radar designed at the

Institute of Applied Physics, Russian Academy of Sciences (IAP RAS). It is a Doppler radar, operating in the X-, C-, and S-bands at frequencies of 10 GHz, 6 GHz, and 3 GHz, respectively, and at vertical transmit/receive (VV) and horizontal transmit/receive (HH) polarizations of electromagnetic waves in each band. The three-band radar operates in a pulse regime radiating 30-ns pulses. The beam width of the radar pattern is about 0.03 rad (X band), 0.05 rad (C-band), and 0.1 rad (S-band). The dynamic range of the radar signal is about 55 dBs in electronic channels, and is enhanced after digital processing. The radar was mounted onboard a research vessel at a height of about 7 m, looking at an incidence angle of 60° and at an azimuth angle of about 40° to the left from the ship's heading. A photograph of a ship based X-/C-/S-band radar is shown in Figure 1.

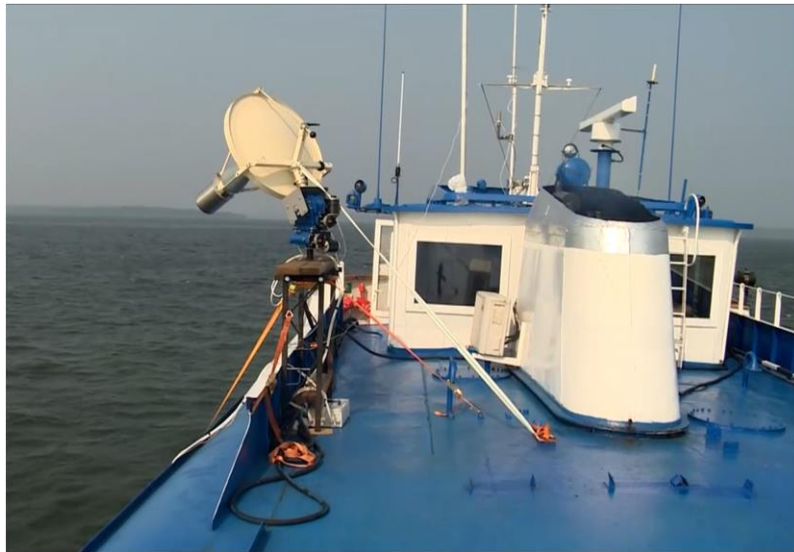


Figure 1. A ship based X-/C-/S-band radar.

The radar footprints and, accordingly, radar spatial resolutions, were as follows: the slant range footprints varied from about 2.8 m in the S-band to 0.8 m in the X-band, and the azimuth range footprints from 1.4 m in the S-band to 0.4 m in the X-band. OLE slick sizes in the experiment were typically 200–300 m, i.e., least two orders of magnitude of the radar footprints. The signal-to-noise ratio (SNR) in the experiments with the three-band radar ranged from about 15–17 dB in the slick to 23–27 dB in the background, depending on radar bands and polarizations.

The wind velocity/direction were measured with an acoustic anemometer (WindSonic[®] Gill Instruments Limited, Lyminster, Hampshire, United Kingdom) mounted onboard the research vessel at a height of about 6 m. Oleic acid (OLE), supposedly simulating natural biogenic films, was used to create film slicks on the water surface. Some amounts of the surfactant (about half a liter of OLE dissolved in one liter of ethanol) were poured on the water from a motor boat to an inflatable trimaran. During the experiments the boat was moving along spiral trajectories creating slicks at least 20 min before satellite overpasses or before slick transects made by the research vessel.

Physical characteristics (the surface tension and film elasticity) of artificial surfactant films used in the experiment were studied in the laboratory using a method of parametric waves [15]. The method is based on measuring the wavelength and the damping coefficient of gravity-capillary standing waves parametrically generated at certain frequencies in a small vertically-oscillating container. From these measurements the surface tension coefficient and the dynamic film elasticity were retrieved (the latter is the main parameter which determines the damping of surface waves). The dynamic elasticity for an oleic acid film retrieved at wave frequencies of 10 Hz, 15 Hz, 20 Hz, and 25 Hz, and the surface tension at a wave frequency of 25 Hz are shown in Figure 2 (cf. [15]). The elasticity of OLE films grows with surfactant concentration and tends to a constant value for a saturated monomolecular

film, which is characterized by dense packing of surfactant molecules oriented nearly vertically on the water surface. At mean surfactant concentrations larger than that of saturated monomolecular films (“oversaturated” films) the excess of surface active materials is contained within microscopic drops, and the dynamic elasticity and surface tension in this case remain practically constant. OLE films in our experiments were normally “oversaturated” and could be characterized by constant elasticity and surface tension values, which were about 25–40 mN/m and 30 mN/m, respectively. Supporting measurements of wind velocity and current profiles, as well as sampling of natural biogenic films from the water surface, were conducted from aboard the trimaran. The physical characteristics of natural films were studied in the laboratory by the method of parametric waves in order to filter out the cases of a highly-contaminated background water surface. In the reported experiments the elasticity of the background biogenic films did not exceed 3–5 mN/m.

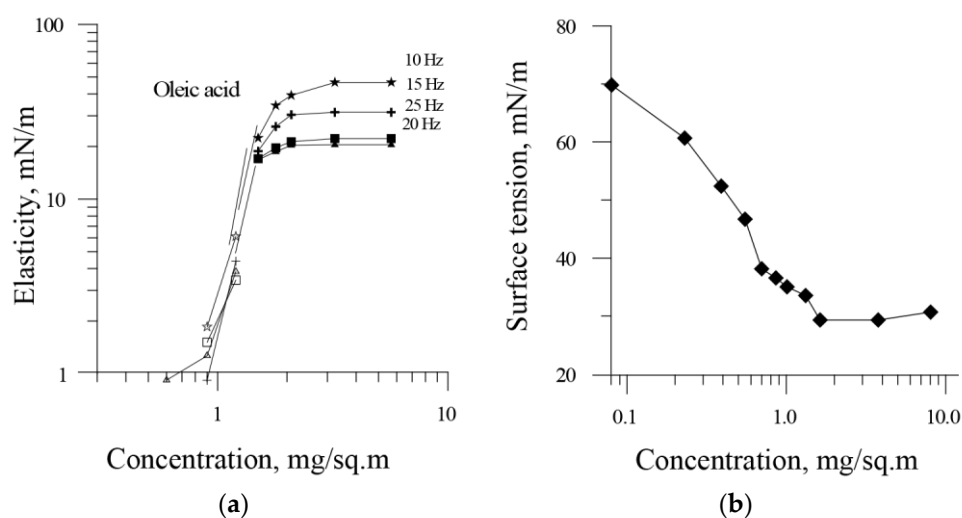


Figure 2. Elasticity at several wave frequencies (a) and surface tension at wave frequency of 25 Hz (b) as a function of the surfactant concentration for OLE films (cf., [15]).

Experiments with artificial slicks were carried out at moderate winds, and wind speeds velocities were in the range of about 5 m/s to 7 m/s. The radar look azimuth angles kV , i.e., angles between the horizontal projection of the incident electromagnetic wave vector and the wind velocity, varied from about 180° (upwind) to 40° from downwind direction. Characteristics of the experiments are summarized in Table 1.

Table 1. Characteristics of experiments on radar probing of OLE film slicks on the Gorky Water Reservoir.

Date, Sensor	Inc. Angle	Wind Velocity, Dir.	Azimuth Angle (kV)	Bragg Wavenumber k_{Bragg} , rad/cm
31.08.2014, TerraSAR-X	37°	7 m/s, NW	(kV) $\approx 40^\circ$ (40° from downwind)	2.43
03.08.2015, TerraSAR-X	32.5°	5 m/s, W	(kV) $\approx 180^\circ$ (upwind)	2.17
22.07.2016, 3-band radar, transect 1	60°	7 m/s, E	(kV) $\approx 80^\circ$	1.01, 2.17, 3.63
22.07.2016, 3-band radar, transect 2	60°	7 m/s, E	(kV) $\approx 40^\circ$	1.01, 2.17, 3.63
22.07.2016, 3-band radar, transect 3	60°	7 m/s, E	(kV) $\approx 180^\circ$	1.01, 2.17, 3.63

3. Results

3.1. Satellite Experiment of 31.08.2014

A fragment of a VV polarization image of an OLE slick in the experiment of 31.08.2014 (TerraSAR-X ascending pass) is shown in Figure 3.

Profiles of NRCS at VV and HH polarizations, BC and NBC contrasts and their ratio for the case of 31.08.2014 are presented in Figure 4. Note, that the contrasts in Figure 4 are current contrasts, which

were calculated as ratios of mean background values, chosen well outside a slick to the current BC or NBC values along a slick transect.

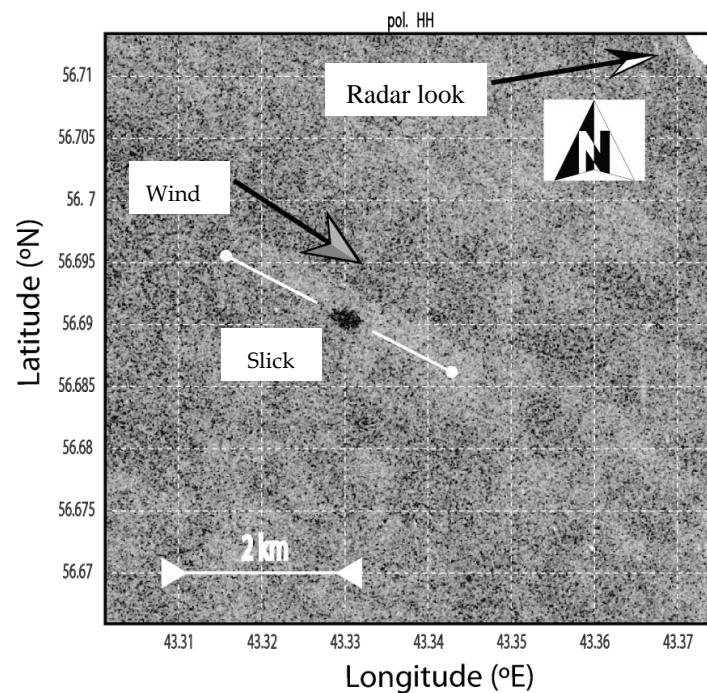


Figure 3. Fragment of the HH image of 31.08.2014 with an OLE slick (a dark spot) in the center. The arrow in the upper right corner denotes the radar look, and the grey arrow in the center is the wind direction. A transect along the slick is shown with the white line segment.

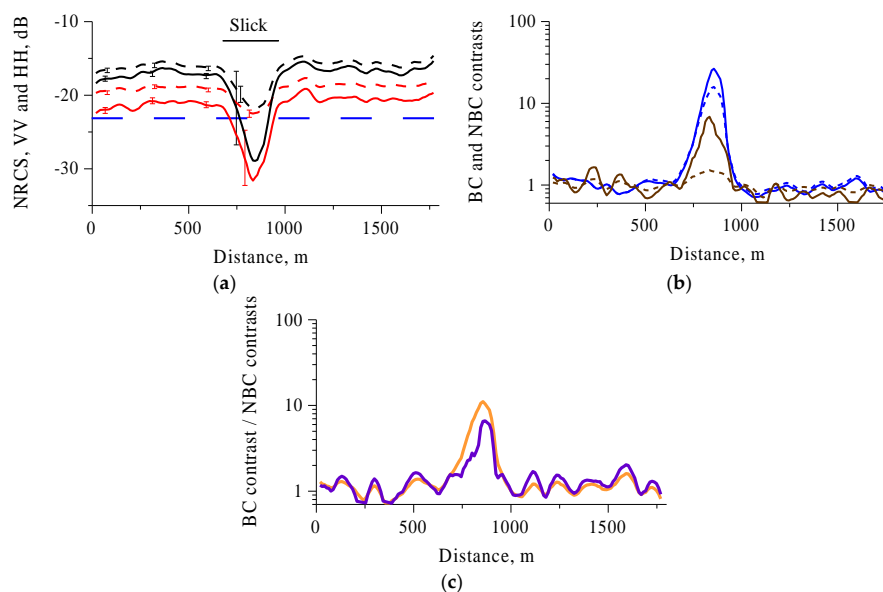


Figure 4. Characteristics of a radar return along the slick transect indicated in Figure 3 for the satellite experiment of 31.08.2014. (a) TerraSAR-X NRCS at VV and HH polarizations (black and red lines, respectively) before and after noise floor subtraction (dashed and solid lines, respectively). The dashed blue line is the noise floor. The vertical bars are a 95% confidence limit. (b) Current contrasts K_{BC} with and without noise floor subtraction (solid and dashed blue lines, respectively) and K_{NBC} with and without noise floor subtraction (solid and dashed brown lines). (c) Contrast ratio K_{BC}/K_{NBC} of radar backscatter with and without noise floor subtraction (violet and orange lines, respectively).

It is seen that the total NRCS drops in the slick by several decibels. The NRCS contrasts, e.g., at VV polarization, are consistent with those obtained in our previous experiments (see, [23]). A drawback of the experiment of 31.08.2014 is that the NRCS values in the slick area are only 1–2 dBs above the noise floor, particularly for HH-polarization. Note that the noise floor is practically the same for both VV and HH polarizations. As a result, the NRCS contrasts after the noise floor subtraction are significantly larger than those without the subtraction and an error of the contrast estimate can be large, so the contrasts in Figure 4 should be considered mostly as rough estimates. Contrasts for the Bragg component, however, are practically unchanged after the noise floor subtraction, while the non-Bragg contrasts are affected by the noise floor. In the considered case the BC contrast is about twice the NBC contrast. The difference between BC and NBC contrasts is even larger if the noise floor is not subtracted.

3.2. Satellite Experiment of 03.08.2015

More reliable contrast estimates were obtained in the experiment of 03.08.2015. A fragment of a VV-polarized image an OLE slick for this case is shown in Figure 5. The slick was elongated due to wind; a slick transect in the image is shown in Figure 5.

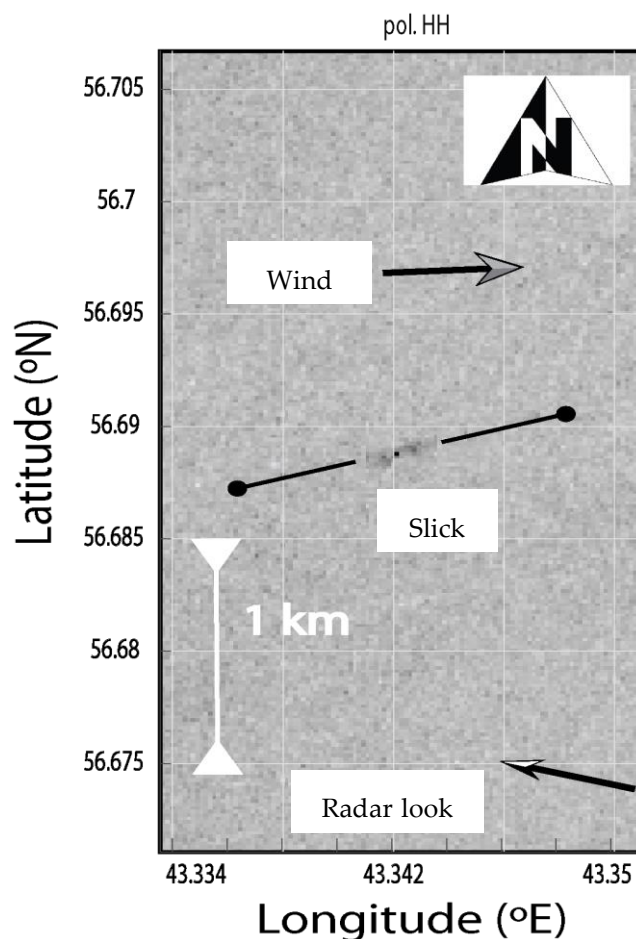


Figure 5. Fragment of a VV polarized image for the experiment of 03.08.2015. The black/white arrow in the bottom right corner denotes radar look, the grey arrow in the upper part denotes the wind direction. Solid and dashed arrows are wind and radar look directions, respectively. A transect along the slick is shown with the black line segment.

An example of NRCS at VV and HH polarizations, as well as Bragg and NBC contrasts and their ratio are shown in Figure 6.

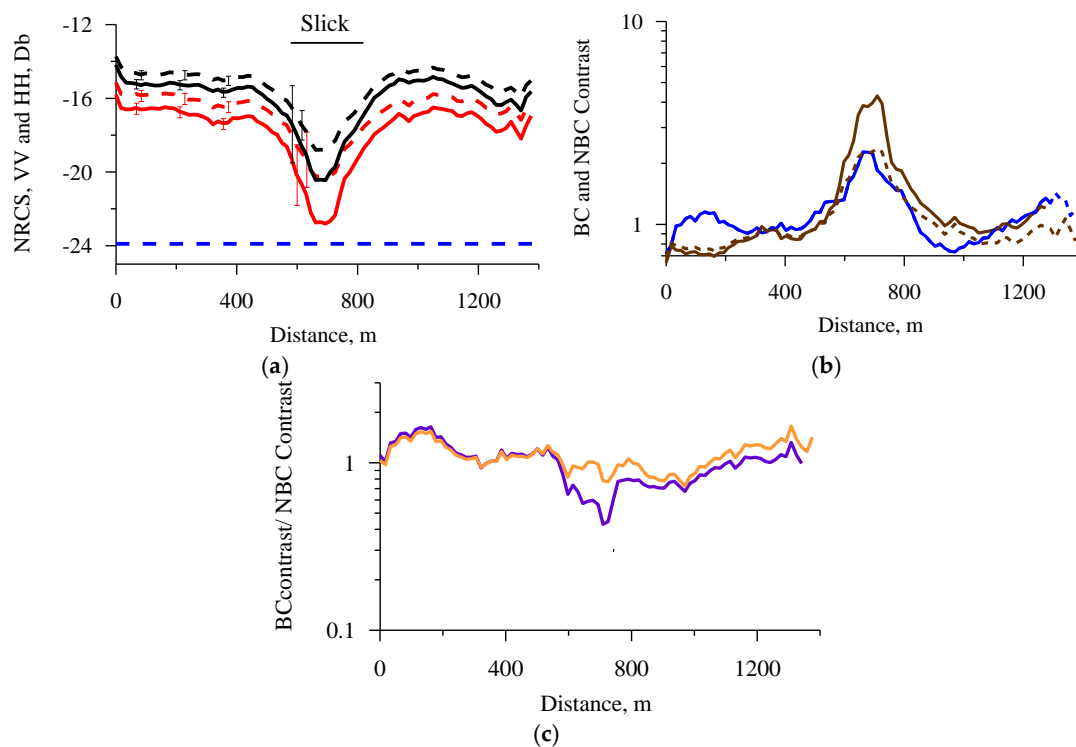


Figure 6. Characteristics of radar returns along the slick transect indicated in Figure 5 for the satellite experiment of 03.08.2015. (a) NRCS at VV-pol and HH-pol before noise floor subtraction (black and red dashed lines, respectively), and after noise floor subtraction (black and red solid lines), the blue dashed line is the noise floor level, the vertical bars are a 95% confidence limit. (b) BC (blue lines) and NBC (brown lines) are current contrasts without noise floor subtraction (dashed lines) and after noise floor subtraction (solid lines). The blue dashed and solid lines are overlapped. (c) Contrast ratio K_{BC}/K_{NBC} (violet: after noise floor subtraction; orange: without noise floor subtraction).

Figure 6 indicates that NRCS both for VV and HH-polarizations for the experiment of 03.08.2015 are well above the noise floor, so that the BC and NBC contrast values are more reliable than for the previous case. It follows from Figure 6c that the NBC contrast, unlike the case of 31.08.2014, is larger than the BC contrast.

3.3. Boat Experiment of 22.07.2016 with a Three-Band Radar

There were three transects through a slick made by a research vessel in order to obtain data at different angles between radar look and wind directions. A scheme illustrating the vessel trajectory and locations of slick transects is shown in Figure 7.

An example of profiles of the radar backscatter at VV and HH polarizations, and of BC and NBC components and their ratios is given in Figure 8 for transect 1, the intensities of radar return in Figure 8 are in arbitrary units, but the same for both VV and HH channels in each radar band.

It is seen that the noise floor of the three-band radar was well below the radar returns in the slick area for both VV and HH polarizations in all bands, so that one can reliably affirm that BC and NBC contrasts are close to each other. In more detail, the NBC contrast in S-band is practically equal to the BC contrast, in C- and X-bands the reduction of NBC is slightly larger than for BC.

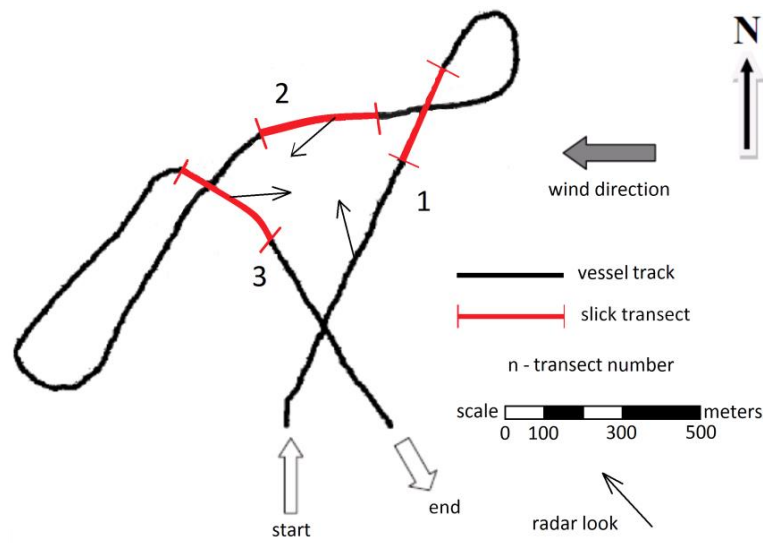


Figure 7. A scheme of a vessel trajectory in the boat experiment of 2016.

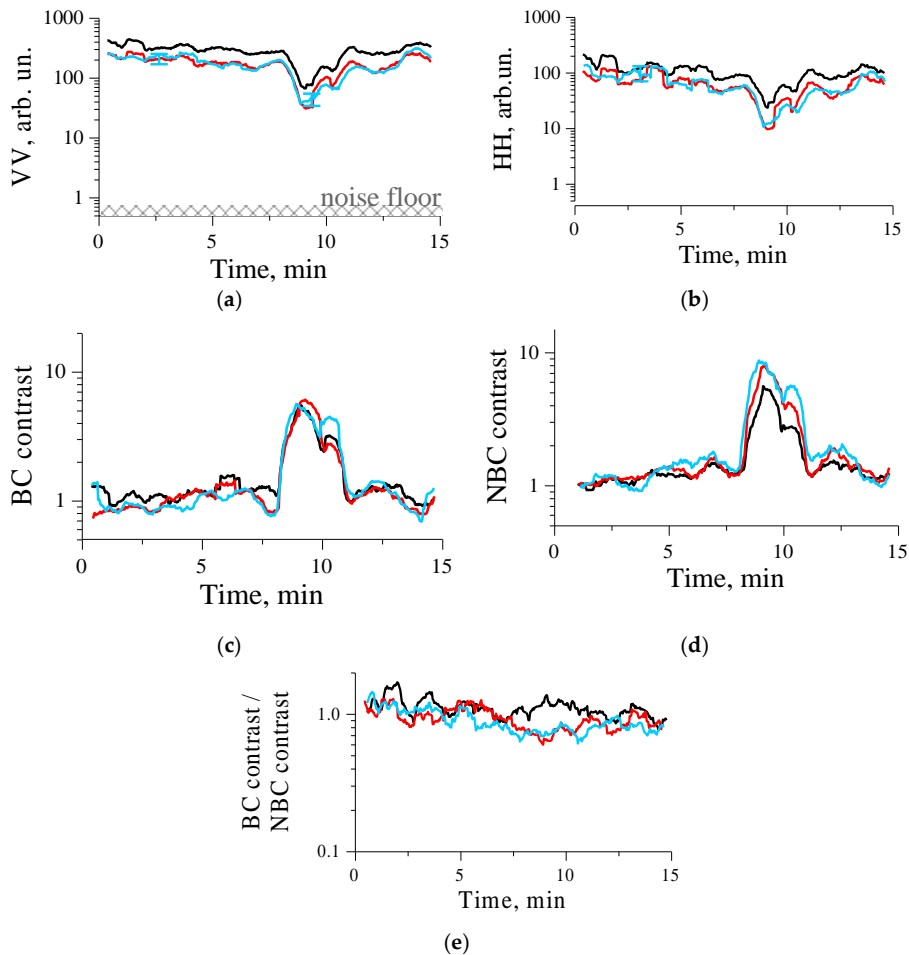


Figure 8. Radar backscatter at (a) VV and (b) HH polarizations (in arbitrary, but the same units) in the boat slick experiment of 22.07.2016 with a three-band radar. Current contrasts K_{BC} (c), contrasts K_{NBC} (d) and K_{BC}/K_{NBC} ratio (e). Black, blue, and red curves correspond to data for S-, C-, and X-bands, respectively. A noise floor level is depicted in (a), and a 95% confidence limit, which is the same for all of the channels, is shown with the vertical bars.

4. Discussion

Let us consider the suppression of different components of radar backscattering estimated from experimental data (see Table 2). Mean contrasts for Bragg and non-Bragg components are presented in Figure 9, and 95% confidence intervals are depicted with the vertical bars. For comparison, some of BC and NBC contrasts obtained with RADARSAT-2 in [33] are shown for similar radar look directions relative to wind direction (kV).

Table 2. Contrasts in slicks for total NRCS at VV and HH polarizations, and for Bragg and NP components in experiments with OLE slicks (see Table 1).

Date, Experiment	Radar Band	k_B , rad/cm	Contrasts				
			K_{VV}	K_{HH}	K_{Bragg}	K_{NBC}	K_{Bragg}/K_{NBC}
22.07.2016 Transect1, (kV) $\approx 80^\circ$	S	1.09	4.3	4.1	4.5	4.1	1.1
	C	2.17	5.4	7.6	4.5	8	0.6
	X	3.63	5.7	8.2	4.6	8.5	0.5
22.07.2016 Transect2, (kV) $\approx 40^\circ$	S	1.09	3.3	3	3.5	3	1.2
	C	2.17	3.9	3.5	4	3.5	1.1
	X	3.63	5	4.2	5.6	4.1	1.4
22.07.2016 Transect3, (kV) $\approx 180^\circ$	S	1.09	4.5	2.3	8.8	2.1	4.2
	C	2.17	8	5.2	9.9	4.9	2
	X	3.63	18	20.5	17.5	20.7	0.8
31.08.2014 TerraSAR-X, (kV) $\approx 40^\circ$	X	2.43	7.4	5.8	9	3.8	2.4
03.08.2015 TerraSAR-X, (kV) $\approx 180^\circ$	X	2.17	2.9	2.5	2.0	3.5	0.6

Figure 9 clearly indicates that BC contrasts increase with wave number, except for the cross-wind case, and are highest for an upwind look direction. Similar behavior can be noted for contrasts in the directions close to the downwind, although the downwind contrasts are somewhat smaller than for the upwind case. The theoretical contrasts for up/downwind cases are estimated according to [2] at the conditions of experiments (at a wind velocity 7 m/s, $E = 20$ mN/m, and at two different empirical coefficient values—0.04 and 0.06 in the formula for a wind wave growth rate (see, [2]). The theory [2] has an obvious drawback of being invalid if the wind wave growth rate is close to the damping coefficient. In our case this occurs at wave numbers larger than 1 rad/cm, so at higher wave numbers the theory can be substituted by an empirical model [20]. Without going into detail of the models one can consider that the reduction of BC radar returns in the slick is due to enhanced viscous damping of short wind waves in the presence of film. This conclusion is also supported by an analysis of cross-wind contrasts. The latter, calculated according to Equation (6), are plotted in Figure 9c. A decreasing tendency of cross-wind BC contrasts with wave number is qualitatively consistent with the experiment. One should note that the elasticity of crude oil films according to recent laboratory measurements [16] has been estimated roughly as 25 mN/m, which is compatible with the OLE film elasticity and, thus, the contrast values [33] shown in Figure 9c can be considered as complementary to our data.

The NBC contrast values and their dependence on the wave number and on the azimuth angle are quite similar to the BC contrasts, thus indicating that film significantly influences the processes of wave breaking. One should recall that strong breaking with crest overturning is typical for surface waves of about 1 m in length and larger. This breaking is supposedly weakly affected by film, since the film can be essentially destroyed due to turbulence and air bubbles in “white caps” mixing down surfactants to the subsurface water layers. The effect of “cleaning” of the water surface in the area of strongly breaking wave crests was demonstrated in our laboratory experiments [34]. It was obtained in [34] when measuring the surface tension in the different phases of m-scale surface waves that, in the presence of OLE-film, the surface tension increased in the area of breaking crests. This proved the effect of film destruction by strong wave breakers.

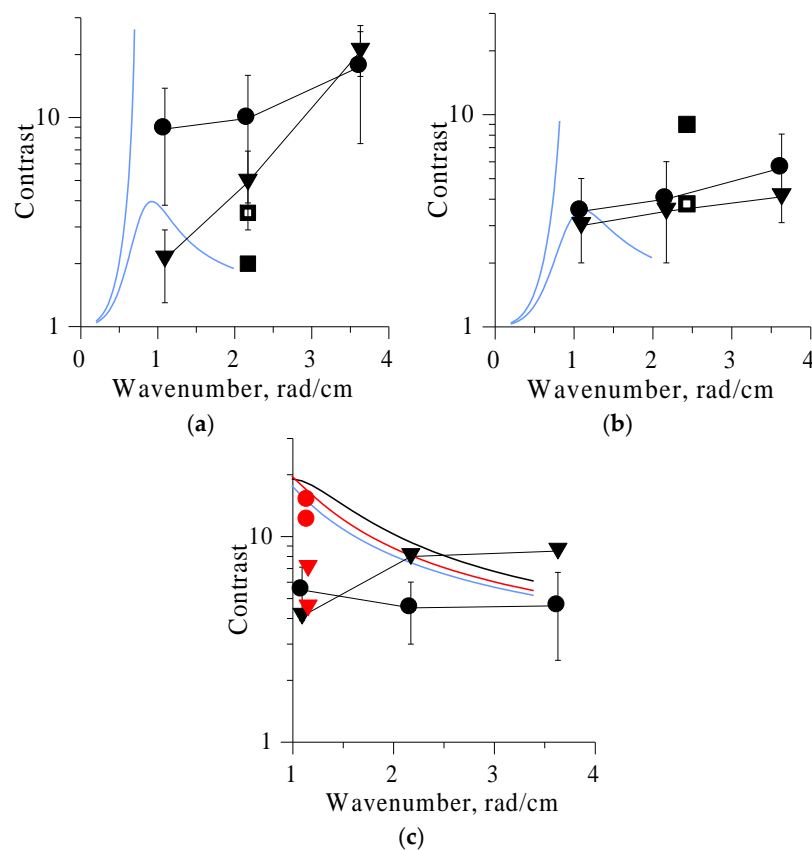


Figure 9. BC and NBC contrasts vs. Bragg wave number for OLE slicks in experiments of 2014–2016 obtained with a three-band radar (●BC, ▼NBC) and with TerraSAR-X (■ BC, □ NBC). (a) Upwind look direction, (b) 40° from downwind, the blue curves: theoretical BC contrasts at two different wind wave growth rates; (c) cross-wind observations; curves: theoretical BC contrasts at elasticity 20 mN/m (black), 30 mN/m (red), and 40 mN/m (blue), the red symbols: Radarsat data [33] for BC (●) and NBC (▼) contrasts for crude oil/emulsion slicks.

One can assume, however, that NBC contrasts in slicks are basically associated with the suppression of wave micro-breaking. The latter is realized for surface waves shorter than 1 m, and micro-breaking features, such as “toe”/“bulge” structures [35] and “parasitic” capillary ripples (see, e.g., [36,37]) occur in the vicinity of wave crests. The structures can be effectively suppressed by film, even at relatively small mean surfactant concentrations. This is because the surfactant concentration $\Gamma(x, t)$ is modulated by the surface wave orbital velocity $U(x - Ct)$ and achieves maximum values near the wave crests. $\Gamma(x, t)$ in the field of a surface wave travelling in the x -direction at a phase velocity C can be written as (see, e.g., [2,4]):

$$\Gamma(x, t) = \Gamma_0 \frac{C}{C - U(x - Ct)} \quad (7)$$

Since $U(x - Ct)$ is in phase with the surface wave elevation, the Γ values increase at the wave crests, of course, if the film is not destroyed due to strong breaking. Accordingly, the surface tension decreases and the elasticity in general increases at the crest. Significant reduction of the surface tension and enhanced elasticity on wave crests results in the abatement of the source of parasitic capillary ripples, i.e., the Laplace pressure [36], and also leads to “smoothing” of the bulge/toe structures. As a result, the quasi-specular reflection of electromagnetic waves from the micro-breaking structures can be strongly reduced.

To study the effect of suppression of micro-breaking in slicks some wave tank experiments have been carried out. Here, first, qualitative results are presented, and a more detailed analysis will be done elsewhere. Our experiments were conducted in an oval wave tank of IAP RAS, where surface gravity-capillary waves were generated with a mechanical wavemaker. The wave steepness was about 0.1 and larger, which corresponded to the generation of parasitic ripples and the formation of toe/bulge structures (see, e.g., [37]). The wave height was measured with a wire gauge and a fine structure of wave profile was studied using photographs. In order to obtain high-contrast wave profiles photo recording in a dark room was performed. A camera was placed opposite the plexiglas tank window. An optical lens system was used to obtain a laser “knife-shape” beam, which was directed downward onto the water. Typical profiles of short gravity waves at two wavelengths (about 10 cm and 20 cm) are depicted in Figure 10. Parasitic capillary ripples were effectively generated by a 10-cm steep wave and were propagating along the forward wave slope. For longer, 20-cm waves a bulge/toe structure dominated. The structures are characterized by rather large slopes, so that quasi-specular reflection of the incident electromagnetic radiation can occur. Film action on the micro-breaking structures was studied using monomolecular OLE-films at concentrations about 1 mg/m^2 . In the presence of film the wave profiles were smoothed and the micro-breaking structures practically disappeared, as illustrated in Figure 10.

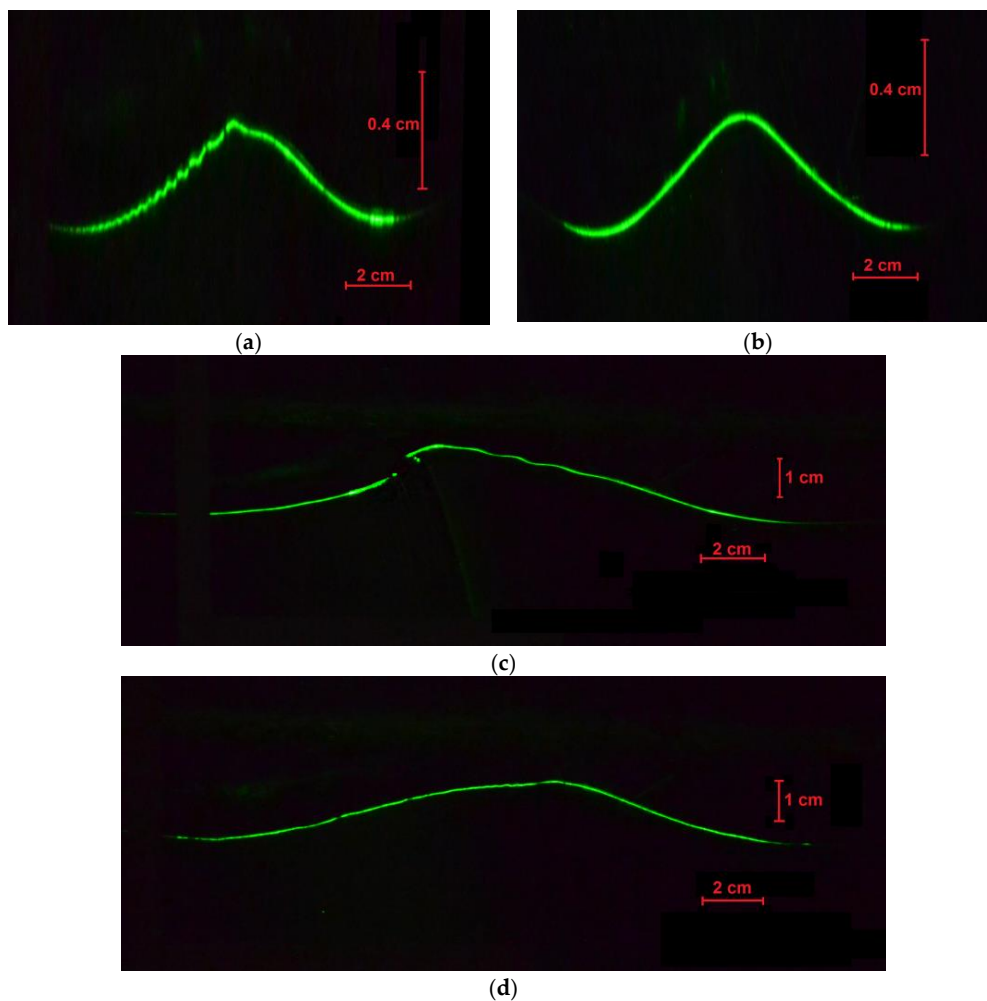


Figure 10. Elevation profiles of steep, short gravity waves of 10 cm (a,c) and 20 cm (b,d) wavelength (left and right columns, respectively), the upper row—clean water (a,b), the bottom row—water contaminated by an oleic acid film (c,d). Waves travel from right to left, and vertical and horizontal scales are extended for clarity.

One can, thus, assume that film can influence micro-breakers more effectively than strong breakers. This influence, however, has been insufficiently studied up to now, as well as the impact of wind on micro-breakers. It has been revealed in wave tank experiments [37] that parasitic ripples in the presence of wind were generated at smaller wave crest curvatures than for mechanically-generated waves. As for bulge/toe micro-breakers, no information about the role of wind in their generation has been found in the literature, and further studies of the dynamics of micro-breakers in the presence of film and wind should be carried out.

5. Conclusions

Organic films of oleic acid deployed on the water surface were observed using dual-polarized TerraSAR-X and an X-/C-/S-band dual-polarized microwave radars. Experiments were carried out at moderate wind (wind velocity about 5–7 m/s), at different azimuth angles, and the incidence angles ranged from about 32 to 60 degrees. The Bragg and non-Bragg components of radar returns were obtained from experimentally measured total radar backscatter at two co-polarizations. Suppression of radar returns of film slicks was characterized by radar contrasts, i.e., by ratios of radar return values for NRCS, BC, and NBC, outside and inside slicks in X- to S-radar bands.

It has been concluded that the Bragg scattering component is suppressed in slicks due to enhanced viscous damping of resonant Bragg cm-scale waves. The contrast values of the Bragg component are highest for an upwind look direction and grow with wave number. The contrasts for downwind directions grow with the wave number, too, but are smaller than for the upwind case. For cross-wind observations, the Bragg contrast values are comparable with up- and downwind contrasts, but slowly decrease with wave number.

An important conclusion is that the non-Bragg component is significantly reduced in slicks. Dependences of the NBC contrasts on radar wave number are qualitatively similar to the Bragg ones, and the NBC contrast values are comparable to ones for BC. Assuming that the non-Bragg component is associated with wave breaking one can conclude that the film essentially influences the wave breaking processes. The effect of the reduction of NBC in slicks can hardly be explained by strong wave breaking which is typical for gravity waves longer than 0.5–1 m since the processes of wave crest overturning can destroy the film. Thus, the action of the film on micro-breaking of cm-dm-scale wind waves and the modification of micro-breaking features—parasitic ripples, and toe/bulge structures—can determine the reduction of NBC in slicks. Although this hypothesis is supported by preliminary wave tank experiments, further studies of an impact of the films on wave breaking processes are to be carried out, aimed to better understand the radar returns from the sea surface and to elaborate the radar imaging models of film slicks.

Author Contributions: S.E. conceived, designed, and took part in the experiments, analyzed the results, and wrote the paper; I.S., J.d.S., and O.S. processed and analyzed the data; and I.K., A.K., and A.M. performed the experiments.

Funding: This research regarding Sections 1–3, Section 5, and partly 4 was funded by the Russian Science Foundation (project RSF 18-17-00224). The results of the laboratory optical measurements of micro-breaking wave profiles presented in Section 4 were obtained by I. Kapustin and A. Molkov in the frame of project 17-05-00448 funded by the Russian Foundation of Basic Research.

Acknowledgments: We are grateful to Jorge M. Magalhaes for codes provided to process SAR data, and to G. Leshchov for his help in the experiment, as well as to O. Danilicheva for her help in the preparation of the paper.

Conflicts of Interest: The authors declare no conflict of interest.

References

1. Alpers, W.; Huehnerfuss, H. The damping of ocean waves by surface films: A new look at an old problem. *J. Geophys. Res.* **1989**, *94*, 6251–6266. [[CrossRef](#)]

2. Ermakov, S.A.; Panchenko, A.R.; Salashin, S.G. Film Slicks on the Sea Surface and Some Mechanisms of their Formation. *Dyn. Atmos. Oceans* **1992**, *16*, 279–304. [[CrossRef](#)]
3. Scott, J.C.; Thomas, N.H. Sea surface slicks—surface chemistry and hydrodynamics in radar remote sensing. In *Wind-Over-Wave Couplings. Perspectives and Prospects*; Sajjadi, S.G., Thomas, N.H., Hunt, J.C.R., Eds.; Clarendon Press: New York, NY, USA; Oxford, UK, 1999; pp. 221–229, ISBN 0-19-850192-7.
4. Da Silva, J.C.; Ermakov, S.A.; Robinson, I.S.; Jeans, D.R.G.; Kijashko, S.V. Role of surface films in ERS SAR signatures of internal waves on the shelf. 1. Short-period internal waves. *J. Geophys. Res.* **1998**, *103*, 8009–8031. [[CrossRef](#)]
5. Gade, M.; Alpers, W.; Hühnerfuss, H.; Masuko, H.; Kobayashi, T. Imaging of biogenic and anthropogenic ocean surface films by the multifrequency/multipolarization SIR-C/X-SAR. *J. Geophys. Res.* **1998**, *103*, 18851–18866. [[CrossRef](#)]
6. Brekke, C.; Solberg, A.H.S. Oil spill detection by satellite remote sensing. *Remote Sens. Environ.* **2005**, *95*, 1–13. [[CrossRef](#)]
7. Minchew, B.; Jones, C.E.; Holt, B. Polarimetric analysis of backscatter from the Deepwater horizon oil spill using L-band synthetic aperture radar. *IEEE Trans. Geosci. Remote Sens.* **2012**, *50*, 3812–3830. [[CrossRef](#)]
8. Levich, V.G. *Physicochemical Hydrodynamics*; Prentice-Hall: Englewood Cliffs, NJ, USA, 1962; ISBN 9780136744405.
9. Lucassen-Reynders, E.H.; Lucassen, J. Properties of capillary waves. *Adv. Coll. Int. Sci.* **1970**, *2*, 347–395. [[CrossRef](#)]
10. Ermakov, S.A. Resonance damping of gravity-capillary waves on the water surface covered with a surface-active film. *Izv. Atmos. Ocean. Phys.* **2003**, *39*, 624–628.
11. Jenkins, A.D.; Jacobs, S.J. Wave damping by a thin layer of viscous fluid. *Phys. Fluids* **1997**, *9*, 1256–1264. [[CrossRef](#)]
12. Ermakov, S.A.; Sergievskaya, I.A.; Gushchin, L.A. Damping of gravity-capillary waves in the presence of oil slicks according to data from laboratory and numerical experiments. *Izv. Atmos. Ocean. Phys.* **2012**, *48*, 565–572. [[CrossRef](#)]
13. Huehnerfuss, H.; Lange, P.; Walter, W. Wave damping by monomolecular surface films and their chemical structure. Pt.II. Variation of the hydrophilic part of the film molecules including natural substances. *J. Mar. Res.* **1984**, *42*, 737–759. [[CrossRef](#)]
14. Loglio, G.; Noskov, B.; Pandolfini, P.; Miller, P. Static and dynamic surface tension of marine water: Onshore or platform-based measurements by the oscillating bubble tensionmeter. In *Marine Surface Films*; Gade, M., Hühnerfuss, H., Korenowski, G.M., Eds.; Springer: New York, NY, USA, 2006; pp. 93–103, ISBN 3-540-33270-7.
15. Ermakov, S.A.; Kijashko, S.V. Laboratory study of the damping of parametric ripples due to surfactant films. In *Marine Surface Films*; Gade, M., Hühnerfuss, H., Korenowski, G.M., Eds.; Springer: New York, NY, USA, 2006; pp. 113–128, ISBN 3-540-33270-7.
16. Sergievskaya, I.A.; Ermakov, S.A. Damping of gravity–capillary waves on water surface covered with a visco-elastic film of finite thickness. *Izv. Atmos. Ocean. Phys.* **2017**, *53*, 650–658. [[CrossRef](#)]
17. Phillips, O.M. Spectral and equilibrium properties of the equilibrium range in the wind-generated gravity waves. *J. Fluid Mech.* **1985**, *156*, 505–531. [[CrossRef](#)]
18. Ermakov, S.A.; Zujkova, E.M.; Panchenko, A.R.; Salashin, S.G.; Talipova, T.G.; Titov, V.I. Surface film effect on short wind waves. *Dyn. Atmos. Oceans* **1986**, *10*, 31–50. [[CrossRef](#)]
19. Donelan, M.A.; Pierson, W.J., Jr. Radar scattering and equilibrium ranges in wind-generated waves with application to scatterometry. *J. Geophys. Res.* **1987**, *92*, 4971–5029. [[CrossRef](#)]
20. Kudryavtsev, V.; Hauser, V.; Caudal, D.; Caudal, G.; Chapron, B. A semiempirical model of the normalized radar cross-section of the sea surface: 1. Background model. *J. Geophys. Res.* **2003**, *108*, 8054. [[CrossRef](#)]
21. Valenzuela, G.R. Theories for the interaction of electromagnetic and oceanic waves—A review. *Bound.-Layer Meteorol.* **1978**, *13*, 61–85. [[CrossRef](#)]
22. Bass, F.G.; Fuks, M. *Wave Scattering from Statistically Rough Surfaces*; Pergamon: Oxford, UK, 1979; 540p, ISBN 9781483187754.
23. Ermakov, S.; Kapustin, I.; Sergievskaya, I.; Da Silva, J.C.B. Remote sensing of oil films on the water surface using radar. In Proceedings of the SPIE, Remote Sensing of the Ocean, Sea Ice, Coastal Waters and Large Water Regions 2012, Edinburgh, UK, 19 October 2012; p. 85320M. [[CrossRef](#)]

24. Phillips, O.M. Radar returns from the sea surface—Bragg scattering and breaking waves. *J. Phys. Oceanogr.* **1988**, *18*, 1065–1074. [[CrossRef](#)]
25. Kwoh, D.S.; Lake, B.M. The nature of microwave backscattering from water waves. In *The Ocean Surface*; Toba, Y., Mitsuyasu, H., Eds.; D. Reidel Publishing Company: Dordrecht, The Netherlands, 1985; pp. 249–256.
26. Kwoh, D.S.; Lake, B.M. A deterministic, coherent, and dual-polarized laboratory study of microwave backscattering from water waves, 1. Short gravity waves without wind. *IEEE J. Ocean. Eng.* **1984**, *OE-9*, 291–308. [[CrossRef](#)]
27. Jessup, A.T.; Keller, W.C.; Melville, W.K. Measurements of Sea Spikes in Microwave Backscatter at Moderate Incidence. *J. Geophys. Res.* **1990**, *95*, 9679–9688. [[CrossRef](#)]
28. Gade, M.; Alpers, W.; Ermakov, S.A.; Huehnerfuss, H.; Lange, P. Wind-wave tank measurements of bound and freely propagating short gravity-capillary waves. *J. Geophys. Res.* **1998**, *103*, 21697–21709. [[CrossRef](#)]
29. Ermakov, S.A.; Kapustin, I.A.; Kudryavtsev, V.N.; Sergievskaya, I.A.; Shomina, O.V.; Chapron, B.; Yurovskiy, Y.Y. On the Doppler Frequency Shifts of Radar Signals Backscattered from the Sea Surface. *Radiophys. Quantum Electron.* **2014**, *57*, 239–250. [[CrossRef](#)]
30. Ermakov, S.A.; Kapustin, I.A.; Sergievskaya, I.A. On peculiarities of scattering of microwave radar signals by breaking gravity-capillary waves. *Radiophys. Quantum Electron.* **2012**, *55*, 239–250. [[CrossRef](#)]
31. Kudryavtsev, V.; Chapron, B.; Myasoedov, A.; Collard, F.; Johannessen, J. On dual co-polarized SAR measurements of the Ocean surface. *IEEE Geosci. Remote Sens. Lett.* **2013**, *10*. [[CrossRef](#)]
32. Skrunes, S.; Brekke, C.; Eltoft, T.; Kudryavtsev, V. Comparing near coincident C- and X-band SAR acquisitions of marine oil spills. *IEEE Trans. Geosci. Remote Sens.* **2015**, *53*, 1958–1975. [[CrossRef](#)]
33. Hansen, M.W.; Kudryavtsev, V.; Chapron, B.; Brekke, C.; Johannessen, J.A. Wave Breaking in Slicks: Impacts on C-Band Quad-Polarized SAR Measurements. *IEEE J. Sel. Top. Appl. Earth Obs. Remote Sens.* **2016**, *9*, 4929–4940. [[CrossRef](#)]
34. Ermakov, S.A.; Kapustin, I.A.; Lazareva, T.N.; Shomina, O.V. Experimental investigation of surfactant film destruction due to breaking gravity waves. Preliminary results. *Sovrem. Probl. Distantionnogo Zondirovaniya Zemli iz Kosmosa* **2015**, *12*, 72–79.
35. Longuet Higgings, M.; Cleaver, R. Crest instability of gravity waves. Part 1. The almost highest wave. *J. Fluid Mech.* **1994**, *258*, 115–129. [[CrossRef](#)]
36. Longuet Higgings, M.S. Parasitic capillary waves: A direct calculation. *J. Fluid Mech.* **1995**, *301*, 79–107. [[CrossRef](#)]
37. Yermakov, S.A.; Ruvinsky, K.D.; Salashin, S.G. Local correlation of the characteristics of ripples on the crest of capillary gravity waves with their curvature. *Izv. Atmos. Ocean. Phys.* **1988**, *24*, 561–563.



© 2018 by the authors. Licensee MDPI, Basel, Switzerland. This article is an open access article distributed under the terms and conditions of the Creative Commons Attribution (CC BY) license (<http://creativecommons.org/licenses/by/4.0/>).